K, where the magnetic structure changes, the Hall conductivity shows clear anisotropy. Such behaviors of the AHE can be successfully ascribed to the Berry phase produced by the spin chirality on the pyrochlore lattice. Our results show that the control of spin texture reflecting lattice topology provides a new way to tailor electronic properties in a variety of magnetic materials in bulk and at interfaces.

References and Notes

1. J. Ye *et al.*, *Phys. Rev. Lett.* **83**, 3737 (1999).
2. K. Ohgushi, S. Murakami, N. Nagaosa, *Phys. Rev. B* **62**, R6065 (2000).
3. R. Karplus, J. M. Luttinger, *Phys. Rev.* **95**, 1154 (1954).
4. J. Kondo, *Prog. Theor. Phys. (Kyoto)* **27**, 772 (1962).
5. P. Matl *et al.*, *Phys. Rev. B* **57**, 10248 (1998).
6. S. H. Chun, M. B. Salamon, Y. Lyanda-Geller, P. M. Goldbart, P. D. Han, *Phys. Rev. Lett.* **84**, 757 (2000).
7. P. W. Anderson, H. Hasegawa, *Phys. Rev.* **100**, 675 (1955).
8. G. Baskaran, P. W. Anderson, *Phys. Rev. B* **37**, 580 (1988).
9. N. Nagaosa, P. A. Lee, *Phys. Rev. Lett.* **64**, 2450 (1990).
10. J. P. Jan, J. M. Gijsman, *Physica* **18**, 339 (1952).
11. R. S. Lee, S. Legvold, *Phys. Rev.* **162**, 431 (1967).
12. A. P. Ramirez, *Annu. Rev. Mat. Sci.* **24**, 453 (1994).
13. B. D. Gaulin, J. N. Reimers, T. E. Mason, J. E. Greedan, Z. Tun, *Phys. Rev. Lett.* **69**, 3244 (1991).
14. M. J. Harris, S. T. Bramwell, D. F. McMorrow, D. F. Zeiske, K. W. Godfrey, *Phys. Rev. Lett.* **79**, 2554 (1997).
15. A. P. Ramirez, A. Hayashi, R. J. Cava, R. Siddharthan, B. S. Shastry, *Nature* **399**, 333 (1999).
16. N. Ali, M. P. Hill, S. Labroo, J. E. Greedan, *J. Solid State Chem.* **83**, 178 (1989).
17. T. Katsufuji, H. Y. Hwang, S.-W. Cheong, *Phys. Rev. Lett.* **84**, 1998 (2000).
18. Y. Oohara, H. Yoshizawa, Y. Taguchi, Y. Tokura, unpublished data.

19. We thank S. Murakami, K. Ohgushi, and N. Hamada for fruitful discussions. Supported in part by a Grant-in-Aid from the Ministry of Education, Japan, and by the New Energy and Industrial Technology Development Organization.

11 December 2000; accepted 22 February 2001

Alignment of Liquid Crystals with Patterned Isotropic Surfaces

Baek-woon Lee and Noel A. Clark*

The molecules of a nematic liquid crystal exposed to an isotropic surface adopt a mean tilt relative to the normal but have no in-plane alignment—that is, they are free to have any azimuthal orientation in the surface plane. Pursuing the theoretical suggestion by Meyer that, in spite of this azimuthal degeneracy, spatially inhomogeneous isotropic surfaces combine with liquid crystal elastic anisotropy to produce alignment, we show that a boundary line between two isotropic regions that differ in mean tilt does indeed align the liquid crystal. The boundaries on a patterned surface of distinct isotropic regions thus act as a system of lines that the molecular orientation locally follows. This enables the development of liquid crystal alignment surfaces based on printing or lithographic patterning.

Nematic liquid crystals (LCs) are fluids made anisotropic by the spontaneous appearance of long-range molecular orientational order. Their resulting birefringence is large and readily controlled by applied fields and surfaces, rendering nematics useful for electro-optical applications. As a result, a key aspect of any LC device or texture is the nature of the surface interactions and geometry that combine to establish its orientation field. LC alignment surfaces used to date, such as mechanical- or photo-buffed polymer films (*1*), evaporated oxide (*2*), crystal surfaces (*3*), or the more recently developed patterned monolayers (*4*, *5*), all require molecular-level in-plane structural anisotropy (*6*) or anisotropic surface roughness (*7*–*11*) to induce molecular orientation. Control of such treatments comes only by way of trial and error, their effectiveness depending on the details of surface structure and molecular arrangement at the nanometer scale that are difficult to predict. Here we demonstrate that LC alignment can be achieved without molecular-scale anisotropy or roughness, showing that a surface lithographically divided into two distinct molecularly smooth isotropic regions can produce alignment governed only by the pattern of boundary lines between them and by the LC elasticity. This observation opens the way to the application of a variety of powerful lithographic and printing techniques to LC alignment, enabling, for example, spatially varying orientation and anchoring strength determined by surface patterning.

Nematic order is described by the unit vector director $\mathbf{n}(\mathbf{r})$, giving the local average molecular long axis direction. In a nematic exposed to an isotropic surface, $\mathbf{n}(\mathbf{r})$ adopts a mean tilt, θ, relative to the normal, but $\mathbf{n}(\mathbf{r})$ is free to have any azimuthal orientation ϕ about the surface normal (Fig. 1). We use binary isotropic surfaces in which the surface area is divided into two distinct regions of differing θ: The surface is either homeotropic (HO), with $\mathbf{n}$ normal to the surface ($\theta = 0°$), or random planar (RP), with $\mathbf{n}$ parallel to the surface ($\theta = 90°$). A cell with boundaries between such surfaces (magenta lines) is shown in Fig. 2, where the local direction of $\mathbf{n}(\mathbf{r})$ is indicated by the blue sticks. The structure of $\mathbf{n}(\mathbf{r})$ in such a cell is established by the interplay of the enforced surface condition on θ with the LC elasticity, which resists spatial variation of $\mathbf{n}(\mathbf{r})$. The elemental local deformations of $\mathbf{n}(\mathbf{r})$, bend (B), splay (S), and twist (T), are indicated by the green areas in Fig. 2 and require an elastic energy density $U_X = (^1/_2)K_X[\partial n_i/\partial s_j]^2$ (where X = S, B, or T) proportional to the respective Frank elastic constant K_B, K_S, or K_T and to the square of the appropriate spatial gradient of $\mathbf{n}(\mathbf{r})$. In general, the elastic constants are not equal, with K_T less than K_B, K_S for known nematics. As a result, in the cell of Fig. 2, the change in orientation imposed at the surface is mediated in the bulk primarily by twist of $\mathbf{n}(\mathbf{r})$, because this is energetically least costly, such that the LC adopts a structure having the mean orientation of $\mathbf{n}$ parallel to the boundary lines. The boundaries of a pattern, then, are a system of lines on the surface which $\mathbf{n}$ locally follows.

Alignment of LCs by spatially inhomogeneous surfaces was proposed by Meyer (*12*) and Berreman (*13*) and demonstrated by Ong, Hurd, and Meyer (*14*), who controlled the mean LC tilt θ by varying the fractional area of $\theta = 0°$ dots in an otherwise planar-aligning ($\theta = 90°$) anisotropic ($\phi = 0°$) obliquely evaporated SiO surface. Also proposed by Meyer (*12*, *14*), and recently analyzed with Landau-deGennes theory (*15*, *16*), is the much more interesting possibility, experimentally realized here, of achieving azimuthal (ϕ) anchoring on isotropic surfaces. Demonstration of these ideas requires elimination of alignment from the molecular interactions and surface topography effects, mentioned above. The surfaces used here were isotropic octadecyltriethoxysilane (OTE) self-assembled monolayers (SAMs) on glass to make the $\theta = 0°$ regions and the surface obtained upon removal of the SAM by exposure to unpolarized, normally incident ultraviolet (UV) light to make the $\theta = 90°$ regions. The frictional and surface relief characteristics of such patterned SAMs were studied extensively by atomic force microscopy (AFM) (*17*, *18*). These data show that both the unexposed SAM and exposed glass areas were isotropic and molecularly smooth. The step in surface relief at the boundaries, on the order of 1 nm high and 100 nm wide, is small enough to

---

Department of Physics, Ferroelectric Liquid Crystal Materials Research Center, University of Colorado, Boulder, CO 80309–0390, USA.

*To whom correspondence should be addressed.

eliminate the possibility of LC alignment by surface topography and enable the study of alignment through elastic anisotropy.

We produced OTE SAMs through the butylamine-catalyzed assembly of $CH_3(CH_2)_{17}Si(OC_2H_5)_3$ (*19*), from solution in toluene onto float glass microscope slides, according to the procedure of Walba *et al.* (*20*). The OTE SAM is hydrophobic (water wetting angle of 111°), giving strong HO LC alignment ($\theta = 0°$) at the surface. For UV exposure, the SAM-covered slides were cut into 1 cm by 1 cm squares, contacted with clips to a chromium–on–fused silica lithographic masks, and the assembly illuminated by unpolarized collimated light from a Hg arc lamp (*21*). After exposure, the sample was rinsed immediately with ethanol to remove the residue. Exposure patterns for alignment were alternating exposed (RP) and unexposed (HO) several-micrometer dimension stripes, as well as the larger areas shown in Fig. 1, the latter enabling detailed study of the alignment achieved on the HO and RP surfaces.

The resulting LC surface-alignment characteristics were studied by polarized transmission visible light microscopy of cells having the LC between parallel plates with the plate spacing $d \approx 10$ μm. The cells were filled by capillarity in the isotropic phase with the British Drug House room temperature cyanobiphenyl nematic LC mixture E31 (nematic-to-isotropic transition temperature $T_{NI} = 61°C$), chosen because its high birefringence ($\Delta n = 0.224$) made it easier to optically probe the LC alignment obtained. The basic alignment mechanism is illustrated in Fig. 1, which shows a cell made with SAM-coated plates having large-scale (100 μm) exposed areas. In the areas where the patterned plates both have a SAM, the LC alignment is HO; with $\mathbf{n}(\mathbf{r})$ along $\mathbf{z}$, the normal to the plates, extinction is observed between the crossed polarizers. In the areas where one plate is exposed, the local LC alignment is hybrid, with $\mathbf{n}(\mathbf{r})$ changing, from a random orientation in the $\mathbf{x}$-$\mathbf{y}$ plane on the exposed surface to HO ($\mathbf{n} \parallel \mathbf{z}$) on the SAM plate, through a distortion involving only splay and bend of $\mathbf{n}(\mathbf{r})$. This structure produces the Schlieren nematic LC texture (Fig. 1B), indicative of the RP alignment on the exposed surface. However, optical observation shows that the orientation at the boundary lines between the exposed and unexposed regions is not random but consistently has its effective optic axes locally parallel and perpendicular to the boundary (Fig. 1B), with the higher refractive index for light polarized parallel to the boundary, as determined by use of a birefringent phase compensator. Thus, the average orientation of the projection of $\mathbf{n}(\mathbf{r})$ onto the $\mathbf{x}$-$\mathbf{y}$ plane is parallel to the one-dimensional (1D) boundary line in its vicinity, which indicates preference for the predominantly twisted director structure near the boundary line, shown in Fig. 2 to mediate between the HO and hybrid regions. The other extreme, where the projection of $\mathbf{n}(\mathbf{r})$ onto the $\mathbf{x}$-$\mathbf{y}$ plane is normal to the boundary line, would involve only splay and bend of $\mathbf{n}(\mathbf{r})$. Figure 2 illustrates the geometrical connection between the azimuthal orientation in the hybrid GLASS-SAM regions (i.e., whether $\phi > 0$ or $\phi < 0$), the orientation of the SAM-GLASS boundary line, and the handedness of the twist. Chiral nematics tend to form the structure of Fig. 2B, which has a preferential twist sense.

The structure of $\mathbf{n}(\mathbf{r})$ at the boundary line between two isotropic surfaces can be calculated from the nematic elasticity (*22*) and the coordinate system of Fig. 1 with, for the HO-RP case, a boundary condition on $\theta(\mathbf{r})$

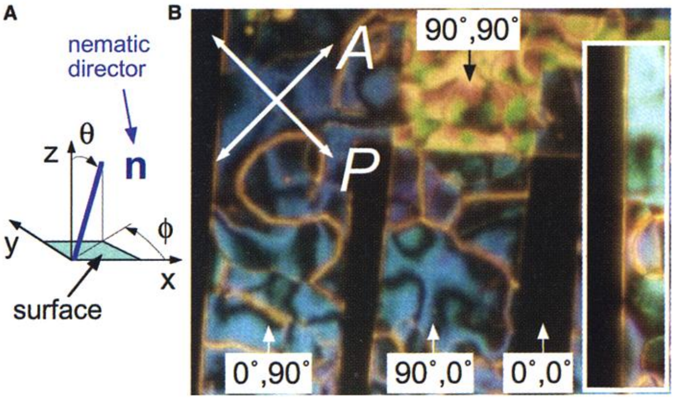

Fig. 1. (**A**) The coordinate system used in the discussion, showing the director $\mathbf{n}(\mathbf{r})$, the mean local molecular long axis ($\mathbf{n} = \mathbf{x}\sin\theta\cos\phi + \mathbf{y}\sin\theta\sin\phi + \mathbf{z}\cos\theta$). (**B**) Nematic LC E31 between SAM-coated plates with large-scale (100 μm) patterning by UV exposure, viewed in transmission between crossed polarizer (*P*) and analyzer (*A*). The field width of (B) is 300 μm. The black areas have neither plate exposed, yielding HO orientation of **n** ($\theta = 0°,0°$, indicating θ on the upper and lower surfaces, respectively). The predominately blue areas have one plate exposed, yielding hybrid orientation of **n**, ranging from RP at the exposed plate to HO on the other ($\theta = 0°,90°$ or $\theta = 90°,0°$). Predominately yellow areas have both plates exposed, yielding RP alignment of **n** through the cell and, thus, higher birefringence ($\theta = 90°,90°$). The RP regions show the characteristic Schlieren texture of disordered nematic (blue/black) and reorientation walls at the surfaces (yellow lines). Note, however, that, for the polarizer and analyzer at 45° to the boundary lines of the exposed areas, the boundary lines are bright (**inset**), a consequence of 90° twist reorientation walls trapped in **n** along the boundary lines.

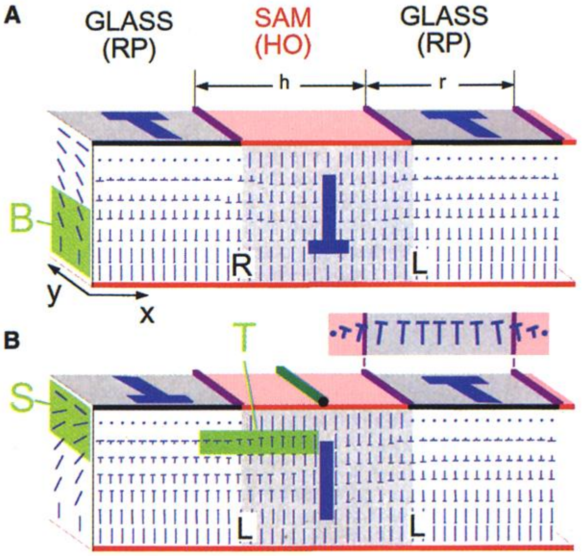

Fig. 2. Schematic of the director structure $\mathbf{n}(\mathbf{r})$ in a LC cell with a pattern of homeotropic (HO) SAM and random planar (RP) GLASS regions patterned onto one surface. The blue lines show the orientation of **n** projected on the surfaces, the "T" bar indicating the end of **n** that projects outward through each surface. The bulk structure of **n** shown is that obtained with $K_T < (K_S + K_B)/2$, for which, in response to the surface orientation change at the boundary lines (magenta), the bulk deformation of **n** is largely twist. The projection of **n** onto the surface plane is then generally parallel to the boundary line, giving the basic orienting effect observed. The handedness of the twist of **n** is directly related to the tilt direction in the splay-bend distortion in the GLASS regions and the orientation of the SAM-GLASS interface. (**A**) $\phi > 0$ everywhere gives opposite handedness [right (R) or left (L)] of twist of **n** on the opposite faces of the SAM region and nonzero tilt of **n** at the center of the SAM region, as indicated by the large ⊥. The mean splay-bend tilt in the glass stripes is indicated on the top surface and is the same on the neighboring glass stripes. This is the structure within the tilt domains of Fig. 3D. **n** remains slightly tilted in the center of the HO (SAM) stripes. (**B**) Uniform left (L) handedness of twist requires change of sign of φ in the center of the HO (SAM) region, where there is no tilt of **n** and a dark band between crossed polarizers (green line). This is the structure of the line-defect boundaries running parallel to the stripes in Fig. 3D. Also shown is the detail of director projection on the glass stripes. The splay rotation in the glass ($\mathbf{x}$-$\mathbf{y}$) plane is a result of saddle splay (K_{24}) elasticity (*24*) and the increasing splay in the $\mathbf{y}$-$\mathbf{z}$ plane upon crossing the SAM-GLASS boundary line.

that has $\theta(x,y,0) = 0$ for $x > 0$ and $\theta(x,y,0) = 90°$ for $x < 0$, and which has $\phi(\mathbf{r})$ unconstrained in the surface plane. The simplest approach to calculation is to first assume elastic isotropy, $K_S = K_B = K_T$, for which $\nabla^2\theta = 0$ determines $\theta(\mathbf{r})$ (*22*), and therefore the nematic energy is independent of ϕ. Thus, for isotropic elasticity, there is no confinement of $\mathbf{n}(\mathbf{r})$ at the surface along the boundary line. However, all known nematics are anisotropic, and for E31, $K_B > K_S > K_T$ (*23, 24*), and the effects of this anisotropy can be incorporated into the analysis as a perturbation by adding a term

$$U_{\text{aniso}}(\phi) = 1/2[K_T - (K_S + K_B)/2]\{\textstyle\int \cos^2\theta\,(d\theta/dz)^2 dxdz\}\sin^2\phi \equiv \gamma_{\text{BI}}\sin^2\phi = \gamma_{\text{BI}}(\mathbf{c}\cdot\mathbf{l})^2 \qquad (1)$$

to the boundary energy per unit length, taking the coefficient in the leading isotropic term to be K_B (*25*). Here **c** is the unit vector projection of the director onto the surface at the boundary line, **l** is the unit vector tangent to the boundary line, and $\gamma_{\text{BI}} \equiv [K_T - (K_S + K_B)/2]\{O(1)\}$. When $K_T < (K_S + K_B)/2$, $U_{\text{aniso}}(\mathbf{c})$ is minimized for **c** parallel to **l** ($\phi = \pm 90°$), and twist walls are stabilized with a line energy $\delta K = K_T - (K_S + K_B)/2$ (*26, 27*).

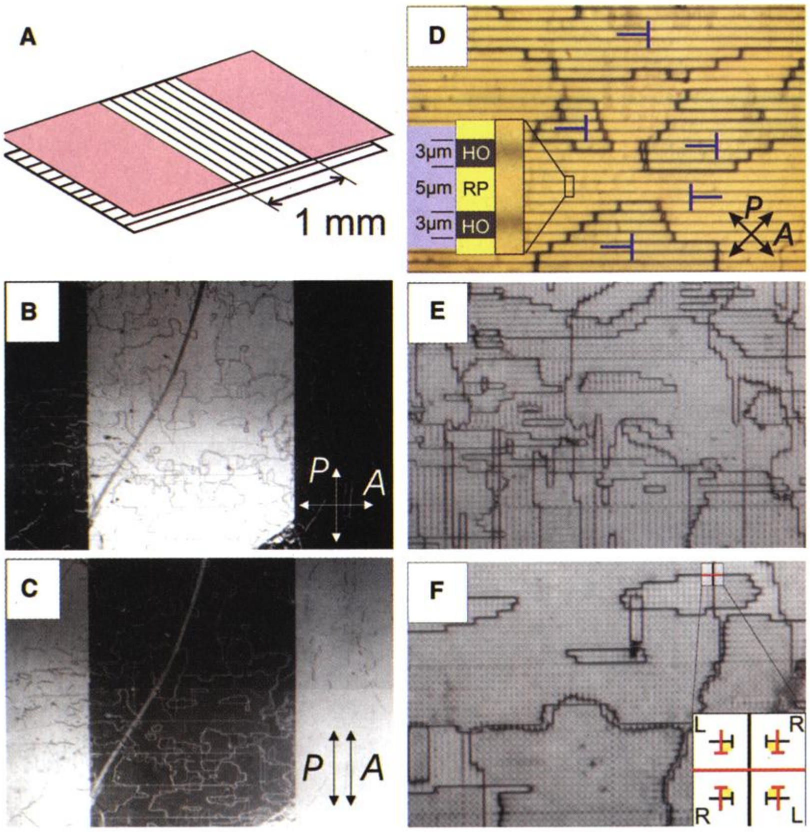

Fig. 3. (**A**) Schematic geometry of a 10-μm-thick E31 nematic cell made with plates that have adjacent unexposed SAM (pink, giving HO orientation) and stripe-patterned areas (giving alignment of **n** at the surface on average parallel to the stripes). The stripes on the two plates are oriented at 90° to one another. (**B**) The left and right areas where there are surface stripes on only one plate extinguish transmitted light with the cell between crossed polarizers oriented parallel or normal to the stripes, behaving as a planar-aligned nematic aligned with **n** parallel to the stripes. This gives extinction between crossed polarizers. (**C**) The central area where the crossed striped overlap extinguishes between parallel polarizers, behaving as a twisted nematic (TN) cell. Both planar-aligned and twisted nematic regions exhibit characteristic topological singularities (disclination loops) in **n**(**r**). The periodically spaced horizontal brighter straight lines are wider HO regions attributable to a step in the stripe pattern periodicity. (**D**) Disclination loops in the region having stripes on only one plate. The darker periodic stripes are over the 3-μm-wide HO regions of a $P = 8$ μm stripe pattern and the bright stripes over the 5-μm-wide RP regions. The blue T's indicate the tilt of **n**(**r**) near the striped surface in the splay-bend deformation that takes **n** from parallel to the surface in the RP areas of the exposed stripes to HO on the unexposed SAM. The disclination lines run parallel to the stripes over HO regions. These are darker because at the disclination, the twist handedness of **n** is the same on both edges of the HO stripes and **n** is perfectly HO over the midline of the stripes. Away from the disclinations, the twist of **n** is of opposite handedness on the two edges of each HO stripe and **n** is slightly tilted over the stripe midplane, giving the HO stripes a slight birefringence. The confinement of the defect lines to run parallel or normal to the stripes is evidence for the boundary-line trapping of **n**. Typical disclination line structure is shown in Fig. 4. (**E**) Disclination loops in the region of overlapping crossed stripes. There are clearly two sets of loops, one on each of the two surfaces, which in (B), (C), and (E) are essentially independent of one another. (**F**) The inset shows that the lines divide the cell into four regions distinguishable by the tilt of **n** at the top and bottom surfaces. As the cell is traversed from one plate to the other, **n** reorients by 90° with a left- (L) or right- (R) handed twist minimizing the elastic energy, depending on the relative tilts in the surfaces, as indicated in the inset. The main panel shows disclination loops in the region of overlapping crossed stripes filled with a weakly chiral nematic [E31 with 3% of chiral CB15 (*30*)] that prefers one-twist handedness. Now the disclinations on the opposite surfaces interact, nearly overlapping to increase the area of the preferred twist at the expense of the other.

The simplest implementation of this alignment scheme is to pattern the surface into HO and RP stripes of widths h and r, respectively, yielding a linear array of boundary lines (Fig. 2). If r is sufficiently small, then the boundary-line alignment dominates the RP regions and the LC alignment will have **n** parallel to the stripes, with an average azimuthal surface anchoring energy/area of $W(\mathbf{c}) = 2U_{\text{aniso}}(\mathbf{c})/(h + r) \sim 10^{-3}$ erg/cm^2 for typical δK (*23*) and stripe pitch $P = h + r \sim 10$ μm. At this P, the magnitude of azimuthal surface anchoring strength is as large as that obtainable through molecular-level structural anisotropy—for example, with rubbed polymer films. However, surface anchoring obtained by patterning can be much more precisely controlled than molecular-level anisotropy. Thus, the surface can be patterned to make the anchoring strength arbitrarily weak, by increasing P, or can be made to have different values and/or directions on adjacent areas of the same surface. Thus, making modern lithographic techniques applicable to LC alignment is a principal advantage of using binary isotropic surfaces.

Alignment in which a HO–planar stripe pattern was used with $P = 8$ μm is demonstrated in Fig. 3, which shows a 10-μm-thick E31 nematic cell made with plates that have alternating stripes of $r = 5$ μm wide exposed RP and $h = 3$ μm wide unexposed HO SAM (*28*). In making the cell, the stripes on the two plates were oriented at 90° to one another, and the stripe areas were only partially overlapped (Fig. 3A), to give the cell a central area of overlapping crossed stripes and side areas with stripes on one surface and SAMs on the other. Figure 3 shows that the one-surface stripe areas extinguish transmitted light with the cell between crossed polarizers oriented parallel or normal to the stripes, behaving as expected for a nematic aligned with **n** along the stripes, whereas the overlap area extinguishes between parallel polarizers, behaving as a twisted nematic (TN) cell (*29*). These extinguishing states are quite dark, indicating good overall alignment. From the existence of the TN structure, we conclude that the alignment potential $W(\mathbf{c})$ is sufficient to withstand the TN twist torque density $\tau \sim K_t/d \sim 10^{-4}$ erg/cm^2.

Both the transmitting and extinguishing

states of Fig. 3, B and C, exhibit line defects in the form of loops that interact strongly with the stripes, as shown in the one-surface stripe region in Fig. 3D and in the TN region in Fig. 3, E and F. The structures of these line defects, which provide direct evidence for the boundary-line trapping of **n**, have been studied in detail and are presented in Figs. 2 and 4. The defects are found to arise from the orientational degeneracies inherent in the boundary-line orientation. The hybrid nematic structure is interrupted by lines where azimuthal orientation of **n** and its apparent tilt from the **x-y** plane switches between the two equal-energy splay-bend possibilities projected on the **y-z** plane in Fig. 2, A and B. This change in mean splay-bend is indicated in the domains of Fig. 3D by the blue T's. In the presence of the boundary lines, the regions of change in the sign of tilt are trapped into lines, which divide into the twist walls of Figs. 2B and 4 running parallel to the stripes, as evidenced by the extinguishing (exactly HO) bands along the center of the HO regions, and the splay-bend defect lines of Fig. 4, jumping between the stripes. The energetically preferred orientation is parallel to the stripes, with the lateral jumps forced by topological necessity. Such a splay-bend defect is a half-space of either a $+2\pi$ (**+1**) or -2π (**−1**) bulk 3D defect line and thus can "escape into the third dimension" (*22*) or terminate on point defects at the black dots in the center of the the RP (GLASS) stripes (Fig. 4). The strong confinement of these defect lines to be near the surface and to run parallel to the stripes is evidence for the preferred orientation of **n** at the boundary lines.

The surface nature of the line defects is evident in Fig. 3E, which shows the cross-stripe TN region at higher magnification. There are two sets of defect lines, one set mediating change of tilt at the upper surface (vertical stripes), and the other at the lower surface (horizontal stripes), identifiable by their tendency to run parallel to the stripes. Although the cell is only 10 μm thick, the two sets of lines barely interact with one another, indicating their confinement to the opposite surfaces. However, the two sets of defect lines can be coupled if the nematic is made slightly chiral by adding a few percent of a chiral compound, in this case CB15 (*30*) (Fig. 3F). The inset in Fig. 3F shows the four structures into which the cross stripe area is divided by the two sets of defect lines. The black line and T's represent the defect line and tilt at the upper surface, whereas the red line and T's represent the defect line and tilt at the lower surface. Each of the four resulting structures has a twist of **n**, with the director rotation as one passes from the upper to the lower plate passing through the quadrant shaded yellow, minimizing the elastic energy by maintaining a uniform tilt through the cell. As indicated, two of the resulting TN domains will be right-handed, and the other two, left-handed. If the nematic is made increasingly chiral—for example, with a right handed twist of **n**—then the right-handed domains will grow in area by displacement of the defect line domain walls to reduce the left-handed area. This response can be seen in Fig. 3F, in the tendency for a defect line on top to overlap one on the bottom, reducing the area of the disfavored sense of twist.

In the domains of uniform mean splay-bend tilt (Fig. 2A), the handedness of the twist changes sign at neighboring boundary lines. However, at the domain boundaries (Fig. 2B), the twist handedness is uniform. Thus, as the nematic is made more chiral—for example, by the addition of a chiral dopant—the density of domain boundaries increases until every stripe is a domain wall, the condition where the chiral nematic twist is commensurately locked onto the stripe pattern. This method for alignment of chiral nematics will be discussed elsewhere (*25*).

The methodology presented here offers a variety of interesting possibilities for novel LC alignment. For example, although the patterning was carried out by UV exposure for the results presented here, we have obtained essentially identical behavior using SAMs obtained by microcontact printing (*31*) onto clean glass. Thus, virtually any complex pattern of nematic alignment, including, for example, heterogeneous patterns for multidomain wide–viewing angle twisted nematic cells, can be fabricated with ease at micrometer resolution. Particularly exciting are the prospects for the fabrication of waveguides by using single stripes and of 2D photonic bandgap structures, either of which could be electrically controlled.

Several additional elements must be incorporated into binary isotropic alignment if it is to become an effective device technology: Comparable results must be obtained on indium–tin oxide and other transparent conducting substrates, and pretilt must be introduced in order to break the tilt degeneracy. The latter should be achievable by using oblique illumination in combination with photoactive SAMs (*32*).

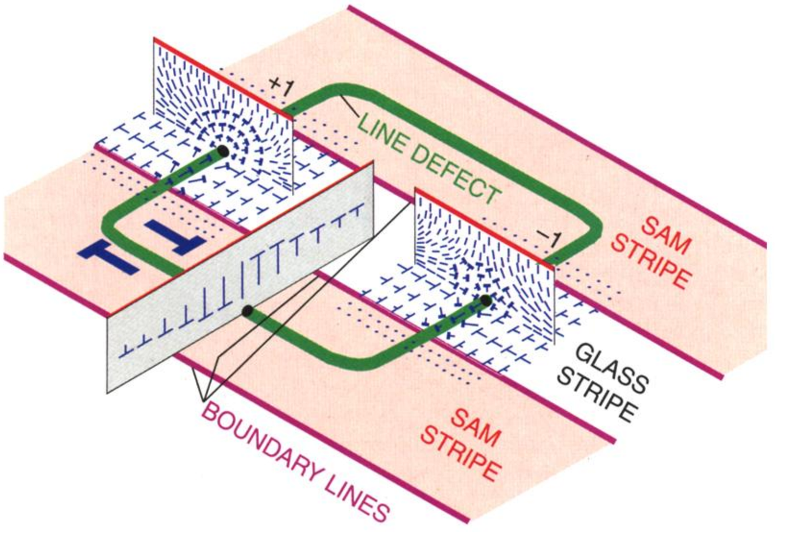

Fig. 4. Schematic of the line-defect loop structure forming the domains of opposite tilt in Fig. 3, D to F. The trapping of **n** at the HO (SAM)–RP (GLASS) boundary forces the defect lines to run parallel to the stripes, where they are twist walls (see Fig. 2B). The short jumps normal to the stripes are splay-bend disclination lines of sign +1 or −1. The splay-bend singularity either escapes into the third dimension or forms a point defect at the black dots in the center of the GLASS stripe. The defect line is confined to the surface region by the trapping of **n** at the boundary line (magenta).

References and Notes

1. J. M. Geary, J. W. Goodby, A. R. Kmetz, J. S. Patel, *J. Appl. Phys.* **62**, 4100 (1987).
2. J. L. Janning, *Appl. Phys. Lett.* **21**, 173 (1972).
3. B. Jerome, *Rep. Prog. Phys.* **54**, 391 (1991).
4. V. K. Gupta, N. L. Abbot, *Science* **276**, 1533 (1997).
5. L. Komitov, G. P. Bryan-Brown, E. L. Wood, A. B. J. Smout, *J. Appl. Phys.* **86**, 3508 (1999).
6. J. Cognard, *Mol. Cryst. Liq. Cryst. Suppl.* **1**, 1 (1982).
7. D. W. Berreman, *Phys. Rev. Lett.* **28** 1983 (1972).
8. S. Faetti, *Phys. Rev. A* **36**, 408 (1987).
9. D. C. Flanders, D. C. Slaver, H. I. Smith, *Appl. Phys. Lett.* **32**, 597 (1978).
10. S. Kumar, B. Cull, Y. Shi, S. Kumar, M. Schadt, *Phys. Rev. E* **53**, 3777 (1996).
11. R. Barberi, M. Giocondo, G. V. Sayko, *Nuovo Cimento* **D16**, 895 (1994).
12. R. B. Meyer, Plenary Lecture, 7th International Liquid Crystal Conference, Bordeaux, France, 1 to 5 July 1978).
13. D. W. Berreman, *J. Phys.* **40**, C3-58 (1979).
14. H. L. Ong, A. J. Hurd, R. B. Meyer, *J. Appl. Phys.* **57** 186 (1985).
15. T.-Z. Qian, P. Sheng, *Phys. Rev. Lett.* **77**, 4564 (1996).
16. ——— *Phys. Rev. E* **55**, 7111 (1997).
17. B. W. Lee, N. A. Clark, *Langmuir* **14**, 5495 (1998).
18. Optimal exposure time was determined as in (*17*) by measurement of adhesion of the SAM to a SiN AFM tip, performed under water to eliminate the capillary force and other possible effects from water vapor in air. Adhesion peaked at about 70 min of UV exposure, which is also when we obtained the best planar alignment; i.e., there is a strong correlation between the adhesive force and the planar anchoring strength. Overexposed surfaces are prone to surface contamination, which often induces HO alignment, and underexposed surfaces induce HO anchoring at low temperature and go through a first-order anchoring transition to planar at temperatures close to the nematic-to-isotropic transition, T_{NI}.
19. United Chemical Technologies, Bristol, PA.
20. J. F. Mooney *et al.*, *Proc. Natl. Acad. Sci. U.S.A.* **93**, 12287 (1996).
21. The UV light from a 200-W Hg lamp was collected by an *f*/1 condenser, 3.8 cm in diameter, producing on the

sample 2.1 W/cm^2 of unpolarized collimated light having a typical Hg arc lamp spectrum. See *Oriel Catalogue* (Oriel, Stratford, CT, 1994), vol. 2, pp. 1–41.

22. P. G. deGennes, J. Prost, *The Physics of Liquid Crystals* (Oxford, London, 1993).
23. E31 is a mixture of cyanobiphenyl homologs, primarily 5-8CB, for which K_B, K_S, and K_T are, respectively, ≈ 25, 17.5, and 8.5 pN (*22*).
24. R. Stannarius, in *Handbook of Liquid Crystals*, D. Demaus *et al.*, Eds. (Wiley-VCH Weinheim, Berlin, 1998), chap. 2.1.
25. B. W. Lee, thesis, University of Colorado, 1998 (Dissertation Abstracts no. 9838378).
26. Addition to the free energy of saddle-splay elasticity, the tendency for opposite sign of splay in orthogonal planes parallel to **n** (*24*, *25*), will cause a rotation of **n** away from the boundary line, the tip of **n** furthest from the surface rotating toward the GLASS region (Fig. 2).
27. We are now in a position to compare this boundary-alignment energy with that arising from the $\delta h \sim 1$ nm surface relief at the SAM-GLASS boundaries. The latter can be obtained from the Berreman formula $\gamma_{relief} \sim 2\pi^3 K(\delta h/w)^2$ (*7*), where $w \sim 100$ nm is the width of the SAM-GLASS boundary region, determined by the wavelength of the UV writing light and measured by AFM in figure 6 of (*17*). $\gamma_{relief} \sim 10^{-3}\gamma_{BI}$ and is thus negligible.
28. The HO-RP boundary positions match the mask boundary positions to within 0.1 μm, as verified by AFM. See (*17*).
29. M. Schadt, W. Helfrich, *Appl. Phys. Lett.* **18**, 127 (1971).
30. CB15 is the British Drug House designation for chiral 4-cyano-4′-(2-methyl)butyl-biphenyl.
31. A. Kumar, N. L. Abbot, H. A. Biebucyk, G. M. Whitesides, *Acc. Chem. Res.* **28**, 219 (1995).
32. K. Ichimura, *Supramol. Sci.* **3**, 67 (1996).
33. Supported by NSF Materials Research Science and Engineering Centers (grant DMR 98-09555) and Army Research Office (grant DAAG55-98-1-0046).

30 November 2000; accepted 27 February 2001

Quantitative Measurement of Short-Range Chemical Bonding Forces

M. A. Lantz,* H. J. Hug, R. Hoffmann, P. J. A. van Schendel, P. Kappenberger, S. Martin, A. Baratoff, H.-J. Güntherodt

We report direct force measurements of the formation of a chemical bond. The experiments were performed using a low-temperature atomic force microscope, a silicon tip, and a silicon (111) 7×7 surface. The measured site-dependent attractive short-range force, which attains a maximum value of 2.1 nanonewtons, is in good agreement with first-principles calculations of an incipient covalent bond in an analogous model system. The resolution was sufficient to distinguish differences in the interaction potential between inequivalent adatoms, demonstrating the ability of atomic force microscopy to provide quantitative, atomic-scale information on surface chemical reactivity.

The atomic force microscope (AFM) was originally intended to be a tool capable of measuring the forces acting between a single pair of atoms (*1*) but has only recently evolved into an instrument capable of producing atomically resolved images of surfaces with characteristic features and defects (*2–4*). This true atomic-scale contrast is generally interpreted as resulting from the short-range chemical interaction between an atomically sharp AFM tip and the nearest atoms on the surface of the sample. In principle, it should therefore be possible to map the chemical bonding potential between the foremost atom on an AFM tip and a specific atom on the sample.

The measurement of short-range bonding forces with the AFM has been difficult to achieve for several reasons. First, at room temperature, thermal drift and piezoelectric scanner creep make it difficult to reliably position the tip above a specific lattice position. Second, most atomic-resolution AFM images have been obtained using a dynamic technique in which the tip-bearing cantilever is driven on its fundamental resonant frequency with a typical amplitude of several nanometers. When the cantilever tip comes close to the sample surface, the force acting on the tip weakly perturbs the cantilever oscillation, giving rise to a small shift Δf in the resonance frequency. The frequency shift is used as a feedback parameter to control the tip-sample spacing, and images therefore correspond to contours of constant frequency shift. Because of the large tip excursion, the relation between the measured frequency shift and the force acting on the tip is not straightforward. Recently, however, progress has been made in quantitatively understanding and inverting this relation (*5–9*). A third difficulty arises because, in general, both short-range forces (such as covalent bonding forces) and long-range forces [such as van der Waals (vdW) and electrostatic forces] act on the tip. Separating these contributions in order to isolate the short-range chemical bonding force is a nontrivial problem. Finally, it is difficult to determine whether the measured chemical force involves more than just a single pair of atoms.

Previously, we demonstrated that the problems of drift and creep can be overcome by working at low temperatures (*10*). In that preliminary work, we acquired constant-height images of the Si(111) 7×7 surface at five tip-sample distances and used the data to construct approximate frequency-versus-distance curves above specific lattice positions. The five data points measured above an adatom site were compared with a frequency shift curve calculated using a first-principles simulation of the short-range force and a simple model for the long-range force. The data were found to be in reasonable agreement with the model, allowing estimation of the maximum attractive force acting on the tip.

Here, we describe quantitative measurements of the short-range chemical bonding force acting between the apex of a silicon AFM tip and specific atomic sites on a Si(111) 7×7 sample. The force is measured over a large range of tip-sample distances using site-specific frequency-distance measurements, which we convert to force-distance data with the use of a recently developed inversion procedure (*7*). The short- and long-range forces are accurately separated by compensating the electrostatic force and measuring the vdW force above nonreactive sites. The magnitude and range of the measured short-range force are found to be in good agreement with first-principles calculations designed to model the same situation (*11*). In addition, we demonstrate that the measured short-range force results from the formation of a single bond. These measurements provide insight into covalent bond formation at surfaces and have implications for understanding the mechanisms responsible for contrast formation in true atomic-resolution AFM.

The experiments were performed using a commercial silicon cantilever, a p-type silicon sample prepared in situ by direct-current heating, and a home-built low-temperature AFM operating in an ultrahigh vacuum (UHV) environment (*10*, *12*). After transfer into the UHV system, the cantilever (*13*) was heated to 150°C for 2 hours to remove absorbed contaminants. To preserve the sharpness of the tip, we applied no additional cleaning procedures; thus, we assume that the tip was initially covered with a native oxide layer. After the microscope was cooled to 7.2 K, imaging was performed in the constant Δf dynamic mode using a constant cantilever oscillation am-

---

Institute of Physics, University of Basel, Klingelbergstrasse 82, CH-4056 Basel, Switzerland.

*To whom correspondence should be addressed. E-mail: mark.lantz@unibas.ch